THE JOURNAL OF

Israel C. Ribeiro, Andreia de Morais, Lucas G. Chagas, Jilian N. de Freitas, Ramiro M. dos Santos, Matheus P. Lima, and Juarez L. F. Da Silva*



Downloaded via UNIV OF SAO PAULO on October 29, 2025 at 10:39:54 (UTC). See https://pubs.acs.org/sharingguidelines for options on how to legitimately share published articles.

Cite This: https://doi.org/10.1021/acs.jpcc.5c04429



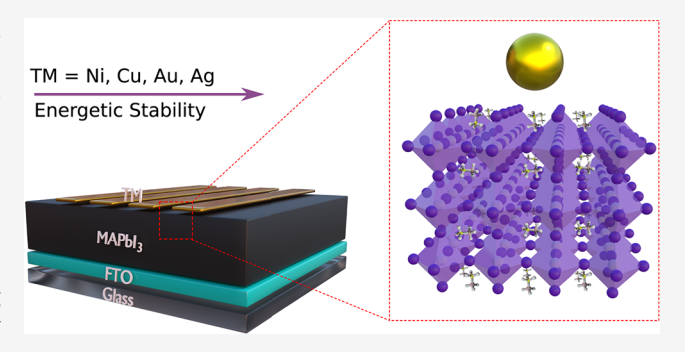
ACCESS I

Metrics & More

Article Recommendations

Supporting Information

ABSTRACT: Perovskite thin films are promising optoelectronic materials because of their low-cost fabrication and high solar cell efficiencies; however, intrinsic defects threaten their stability and scalability by activating degradation pathways. Here, we combine density functional theory calculations with experimental characterization to study the adsorption of transition metals (TMs: Ni, Cu, Ag, Au) on pristine and defect-engineered MAPbI₃(100) surfaces passivated with methylammonium (MA) cations. Our calculations indicate that subsurface TM substitution is energetically less favorable than surface adsorption, with strong TM-I bonding playing a key role in stabilizing the doped systems. This stability follows the trend Ni > Cu > Au > Ag, highlighting the relative



preference of different TMs in interactions with the perovskite structure. Moreover, the presence of iodine vacancies and MA significantly alters both the energetics of adsorption and the electronic structure of the perovskite. Charge analysis demonstrates that Ag, Au, and Cu function as electron donors, resulting in a shift of the Fermi level toward the conduction band, which could enhance the charge transport properties of the material. Reductions in work functions after adsorption suggest that TMs not only enhance surface passivation, but also contribute to lowering electron-extraction barriers, with Cu showing the most pronounced effect in this regard. Complementary field emission scanning electron microscopy and energy-dispersive spectroscopy analyses of TM-coated MAPbI₃ substantiate these findings, revealing distinct metal distributions and demonstrating that Ni achieves the highest surface uniformity, consistent with our computed adsorption energies. These insights advance our understanding of TM-perovskite interactions and support future strategies aimed at enhancing both the stability and performance of perovskite-based photovoltaic

1. INTRODUCTION

Metal halide perovskites have swiftly advanced as leading contenders in the domain of photovoltaic research, predominantly due to their low fabrication costs and significant advancements in power conversion efficiency (PCE) over the past 20 years. Their exemplary optoelectronic properties, which include high defect tolerance within the bulk region,³ robust light absorption, and efficient charge transport, render them as excellent candidates for future solar energy technologies. Nevertheless, surface defects continue to pose a substantial obstacle, undermining the structural integrity and optoelectronic stability of thin films at the interfaces and obstructing the large-scale commercialization of perovskite solar cells (PSCs).^{3,6,7}

Three-dimensional (3D) perovskites follow to the archetypal formula ABX3, 8,9 characterized by a framework of cornersharing BX₆ octahedra. Within this structure, a divalent metal cation (B) is octahedrally coordinated by halide anions (X), while a monovalent cation (A) occupies the interstitial positions between the octahedral network. A classical example of ABX₃ is MAPbI₃, which includes a methylammonium cation (CH₃NH₃⁺) located at the A site, lead (Pb²⁺) located at the B site, and iodide (I⁻) positioned at the X site. Multiple studies have elucidated that MAPbI3 manifests several temperaturedependent polymorphic forms, spanning orthorhombic, tetragonal, cubic, and hexagonal phases, each exhibiting distinct structural and electronic properties that critically affect device performance. 10-12

Despite these advantageous properties, the achievement of large-area, uniform perovskite films persists as a significant impediment to scale-up. 13,14 Transparent conductive oxide (TCO) substrates, notably indium tin oxide (ITO) and fluorine-doped tin oxide (FTO), present additional perform-

Received: June 26, 2025 Revised: October 13, 2025 Accepted: October 20, 2025



ance limitations due to their high sheet resistance, thereby intensifying resistive losses and enlarging the efficiency gap between laboratory-scale devices and commercial modules. ^{13,16} Although scalable deposition techniques, such as blade and slot-die coating, have made advancements in enhancing film uniformity, they continue to be obstructed by material wastage and elevated production costs. ¹³ Vacuum-based deposition methodologies, including thermal evaporation and sputtering, offer the potential for better material utilization and film quality; nevertheless, their efficacy remains constrained by the inherent resistivity of TCOs. ^{13,17}

A promising approach to mitigate these resistive challenges is the integration of metallic grids into TCO substrates to improve conductivity and minimize ohmic losses. ^{13,18} These grids, which are generally fabricated via sputtering or printing methods, have facilitated significant advancements in both rigid and flexible PSCs. ^{19–21} Recent evidence demonstrating Ag-based grid architectures achieving unprecedented efficiencies in flexible devices highlights their potential for industrial implementation. ²² However, the prolonged stability of these metallic grids under operational conditions remains insufficiently investigated, presenting a considerable obstacle for the reliability and scalability of perovskite-based modules. ¹⁹

da Silva Filho et al. 13 conducted a systematic evaluation of the stability of various metallic grids in contact with perovskite layers, successfully identifying materials that demonstrate significant morphological and electrical resilience during the processing stages. Metals such as Ni, Pd, Pt, and Ta were identified as highly stable candidates for constructing robust electrode architectures. Although Al showed susceptibility to degradation under conventional cleaning protocols, its stability can be enhanced by employing adhesion layers. Among the metals assessed, Ni emerges as a particularly promising option, owing to its cost-effectiveness, high conductivity, and favorable alignment of the work function with standard TCO energy levels, thus providing a pathway toward scalable and durable perovskite photovoltaics.

Complementary investigations conducted by Lin et al.²³ have demonstrated that the targeted surface doping of perovskites with specific transition metal ions can adjust carrier concentrations by as much as 8 orders of magnitude. The process of bulk doping remains problematic due to the inadequate incorporation of metal ions into the lattice, frequently resulting in dopant segregation. Nevertheless, precise optimization of doping concentrations facilitates the emergence of grain-boundary homojunctions, which advance charge separation and mitigate recombination losses. This methodology not only augments photovoltaic efficiency but also unveils novel prospects for thermoelectric devices by capitalizing on the inherently low thermal conductivity of doped perovskite systems. The interface between metallic grids and perovskite thin films subsequently constitutes a crucial frontier for optimizing performance. The adsorption of metallic species can effectively initiate doping on the perovskite surface, thereby altering carrier dynamics, including mobility and recombination pathways, which in turn affects the longterm stability of the device. ²³ Although metallic grids significantly enhance conductivity, their integration must be meticulously designed to prevent adverse alterations to the electronic structure of the active layer.

In this investigation, we synthesize theoretical simulations alongside experimental characterization to investigate the adsorption of transition metal adatoms on MAPbI₃ surfaces

passivated with MA cations. Our computational results demonstrate a substantial dependence of adsorption energetics and electronic effects on both the metal species and the local surface environment. Specifically, Ni exhibits the strongest binding affinity and robust TM–I coordination. The existence of surface vacancies, particularly $V_{\rm MA}$ and $V_{\rm L}$, significantly influences the adsorption strength and electronic structure, while surface adsorption is generally more favorable than subsurface substitution. The adsorption of Cu and Ni significantly modifies the work function and charge distribution at the interface, corroborating experimental findings that Ni achieves the most uniform spatial distribution across perovskite films. These findings emphasize the interaction between surface chemistry and device architecture, offering fundamental insights for the design of durable and high-performance PSCs.

2. THEORETICAL APPROACH AND COMPUTATIONAL DETAILS

2.1. Total Energy Calculations. Our calculations were performed within the framework of spin-polarized density functional theory (DFT), 24,25 employing the semilocal Perdew-Burke-Ernzerhof (PBE) formulation²⁶ for the exchange-correlation energy functional. While standard DFT-PBE has been extensively used for the design and characterization of a wide array of materials, 8,27-29 it is well recognized that it does not accurately account for long-range nonlocal van der Waals (vdW) interactions. This shortcoming impairs the predictive accuracy regarding interlayer binding energies and equilibrium separations in layered materials,³⁰ adsorption characteristics of molecular entities on solid surfaces, ^{32,33} and the interaction of organic monovalent cations within hybrid perovskite lattices. 34,35 To mitigate these limitations while preserving computational efficiency, the semiempirical Grimme D3 correction was employed,³⁶ which offers an enhanced description of the vdW interactions.

The Kohn–Sham (KS) wave functions were expressed using plane-wave basis sets, with electron–ion interactions characterized by the projector augmented-wave (PAW) method, 37,38 as implemented in the Vienna Ab Initio Simulation Package (VASP), version 5.4.4. 39,40 The equilibrium geometries of MAPbI₃ slabs terminating in MA molecules, for surface passivation, were derived through the concurrent relaxation of both in-plane stress components (xy) and atomic positions (xyz), 41 adopting a plane-wave cutoff energy of $1.50\times EN-MAX_{max}$ denoted as 631.353 eV. In this context, $ENMAX_{max}$ refers to the maximum recommended cutoff energy specified by the PAW projectors.

Subsequent evaluations of properties, including interaction energies, electronic band structures, density of states (DOS), work function, absorption spectra, and net atomic charges (calculated using the density-derived electrostatic and chemical method, DDEC6), 42,43 were conducted employing a slightly reduced plane-wave cutoff of 473.515 eV, which exceeds ENMAX $_{\rm max}$ by 12.5%, and therefore yields excellent convergence for total energies and electronic states. Brillouin zone integrations were executed using a Monkhorst–Pack 2 \times 2 \times 1 k-point grid for structural relaxations and a more refined 4 \times 4 \times 1 k-grid for computations involving electronic and optical properties. All structural optimizations converged when the residual forces acting on all atoms were reduced below 2.5 \times 10 $^{-2}$ eV Å $^{-1}$, concomitant with an electronic self-consistency threshold of 10 $^{-5}$ eV in total energy.

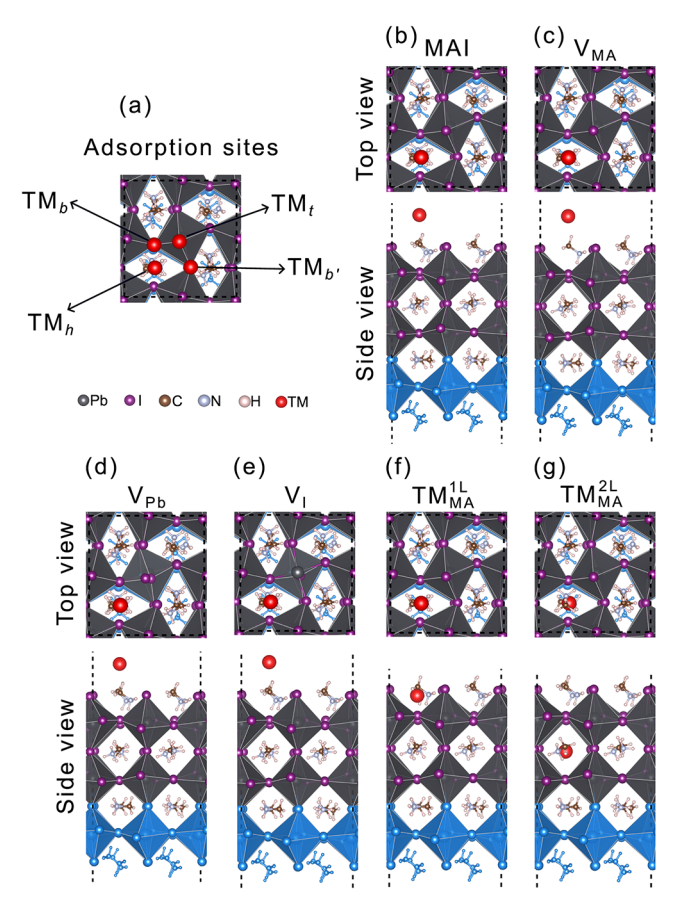
Article

2.2. Perovskite Thin Film Models. 2.2.1. Passivated Surface Model via MA Molecules. To begin, a 3D orthorhombic $(2 \times 2 \times 2)$ bulk supercell was used to construct a 2D orthorhombic (2×2) surface (100) slab model containing 3 octahedral layers separated by a vacuum region of 15 Å from the repeated slabs (periodic boundary condition), i.e., the vacuum region is used to prevent spurious interactions between the slab periodic images, thereby isolating the surface under investigation. The resulting perovskite thin film (slab), forms a slab with the unit cell chemical MA₁₆Pb₁₂I₄₀ formula, where 8 MA belongs to the thin film structure and 8 MA molecules are used to passivate the charges of the PbI₆ octahedra, i.e., particular attention was required for surface charge compensation.²⁹ For example, according to the electron counting rule, each surface of the slab (top and bottom) requires 4 MA⁺ cations (electron donors) for complete surface passivation of the inner slab atoms, that is, $8MA^+ + 12Pb^{2+} +$ 40I-. The resulting passivated configuration is here called the MAI model due to its surface terminations. To mitigate issues associated with a net dipole moment in the supercell in DFT calculations, the bottom surface of the slab was fixed during calculations involving adsorption of the TM species, thereby emulating adsorption on an extended perovskite substrate.

2.2.2. Transition Metal Adsorption on Passivated Slabs. In Figure 1(a), the adsorption sites on the (100) surface model are depicted, including the hole (h), bridge (b), and top (t)sites, which are determined by the positions of the terminal iodides. To accommodate the two distinct bridge-site configurations, an additional site, b', has been incorporated. Consequently, each Ni, Cu, Ag, and Au species was adsorbed at one of the designated high-symmetry sites on the top surface of the slab MAI, as illustrated in Figure 1(b).

2.2.3. Transition Metal Adsorption on Defective Slabs. To investigate the influence of vacancies on the adsorption properties of transition metals in perovskite films, we have constructed defective slabs (100) with vacancies, specifically vacancies of methylammonium (V_{MA}) , lead (V_{Pb}) , and iodide $(V_{\rm I})$ in the upper surface layer within model MAI, as illustrated in Figure 1(c-e). All DFT calculations were performed for neutral configurations, that is, q = 0, as charged-state calculations for surface slabs are well beyond the scope of the present manuscript. Furthermore, in such systems, compensating background charges result in an unphysical divergence of the total energy with an increase in vacuum thickness. Concentrating on neutral defects eliminates these artifacts and facilitates a credible evaluation of the local chemical bonding between the transition metal adatom and the defect site.44,45

2.2.4. Transition Metal Subsurface Incorporation. Under particular conditions, TM species can also be placed at subsurface sites, which could play a significant role in the degradation of perovskite thin films.²³ This study involves the investigation of slab models in which TM species are integrated as substitutional entities at positions MA, Pb, and I within subsurface regions near the surface. Incorporation was performed in both the first (TM_s^{1L}) and second (TM_s^{2L}) atomic layers of the slab, where s denotes the sublattice sites MA, Pb, or I, as illustrated in Figure 1(f),1(g). The notation used throughout the manuscript was influenced by the Kröger-Vink notation.⁴⁶ To distinctly separate local chemical bonding from erroneous electrostatic interactions encountered in charged 2D periodic systems, this research investigates the adsorption and



pubs.acs.org/JPCC

Figure 1. Molecular representation for the perovskite model systems: (a) Adsorption sites of transition metal (TM) adatoms (Ni, Cu, Ag, and Au) on the surface of the MAI slab model. Top (t), bridge (b, b'), and hollow (h) adsorption configurations were systematically investigated. As a representative case, the figure illustrates TMh adsorption on both (b) MAI and defective surfaces, including (c) vacancies at methylammonium (V_{MA}) , (d) lead (V_{Pb}) , and (e) iodide $(V_{\rm I})$ sites. Surface adsorption was also examined at MA, Pb, and I sites, with the MA site shown here as an example for the (f) surface (TM_{MA}^{1L}) and (g) subsurface (TM_{MA}^{2L}) adsorption. Blue atoms indicate the fixed bottom surface, and the dashed line outlines the unit cell.

subsurface incorporation of an electrically neutral TM atom onto a neutral vacancy site.

3. RESULTS AND DISCUSSION

As indicated previously, an extensive series of DFT-PBE+vdW calculations were executed, and various physicochemical properties were computed to operate as descriptors for characterizing the effects of metal-species adsorption on both ideal and modified perovskite surfaces. Herein, we will discuss the most significant findings, while additional results are detailed in the Supporting Information.

3.1. Energetic Stability via Adsorption and Interaction Energies. In order to assess the stability of adsorbed single TM species in thin perovskite films (slab model), we calculated the adsorption energies (E_{ad}) of the selected TM species located at several surface adsorption sites, as indicated in Figure 1, namely h, t, b, and b', as well as subsurface incorporation (substitution) at the lattice positions MA, Pb and I in first (TM_s^{1L}) and second (TM_s^{2L}) layers. E_{ad} is given by the following equation

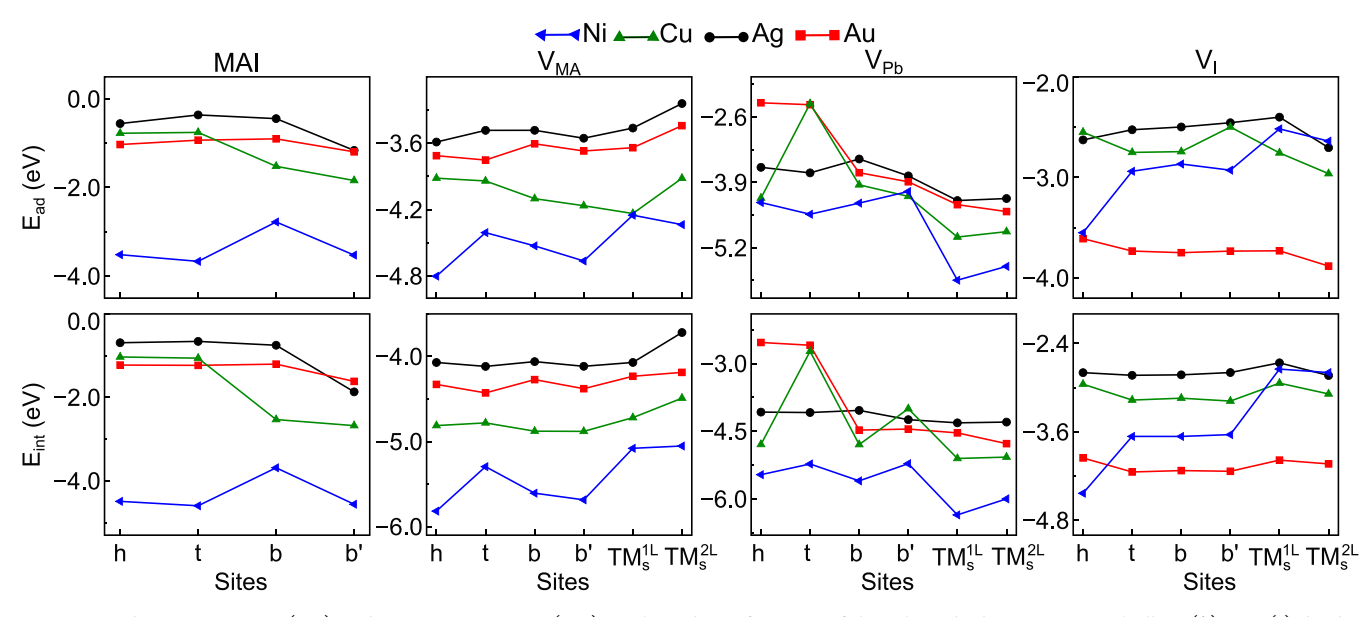


Figure 2. Adsorption energy (E_{ad}) and interaction energy (E_{int}) , evaluated as a function of the selected adsorption sites: hollow (h), top (t), bridge (b), and alternate bridge (b'), of single-transition-metal (Ni, Cu, Ag, and Au) on MAI, V_{MA} , V_{Pb} , and V_{I} surfaces models, as well as for subsurface substitution at MA, Pb, and I sites in the first (TM_{s}^{1L}) and second (TM_{s}^{2L}) layers of perovskite thin films.

$$E_{\rm ad} = E_{\rm tot}^{\rm TM/slab} - E_{\rm tot}^{\rm slab \; relaxed} - E_{\rm tot}^{\rm TM \; free \; atom}$$
 (1

where $E_{\rm tot}^{\rm TM/slab}$ is the total energy of the thin films considering the adsorption of TM, while $E_{\rm tot}^{\rm slab}$ relaxed is the total energy of the optimized perovskite slabs with fixed lattice parameters, relaxed only with respect to the internal atomic positions and without TM adsorbates, $E_{\rm tot}^{\rm TM}$ free atom is the total energy of the free TM.

In addition, to assess the strength of the interaction between the thin film and the TM, we calculate the interaction energies (E_{int}), as defined by the following equation

$$E_{\rm int} = E_{\rm tot}^{\rm TM/slab} - E_{\rm tot}^{\rm slab \; frozen} - E_{\rm tot}^{\rm TM \; frozen}$$
 (2)

By excluding the contributions of the individual components by evaluating $E_{\rm tot}^{\rm Slab}$ frozen and $E_{\rm tot}^{\rm TM}$ frozen, which correspond to the total energies of the film and TM frozen in their optimized positions, it is possible to measure the important relaxation effects due to the adsorption of the adsorbed species.

The negative values of $E_{\rm ad}$ and $E_{\rm int}$ for both surface adsorption and subsurface substitution indicate energetically favorable adsorption and interaction between the TM and the perovskite surface, see Figure 2. However, the degree of interaction is strongly dependent on both the choice of metal and the specific adsorption or subsurface substitution site, leading to pronounced variations in the binding strength across the slab.

3.1.1. Adsorption of TM on MAI Slabs. In the MAI model, both $E_{\rm ad}$ and $E_{\rm int}$ follow a consistent trend, with Ni showing the most negative values, highlighting its exceptionally strong interaction with the surface. Among the adsorption sites, the t site yields the highest stability for Ni. In contrast, Ag interacts most strongly at the b' site, with the t site being the least favorable. In particular, Au and Cu display site preferences similar to Ag, although with generally stronger interactions at the b' site.

3.1.2. Adsorption of TM on Defective Slabs. Vacancies, on the other hand, induce significant variations in the adsorption behavior of TM on surfaces, depending on the specific adsorption site. In the case of $V_{\rm MA}$, the vacancies exhibit a more favorable $E_{\rm ad}$ for Ag at the h site, whereas the t site

produces an even stronger interaction when considering $E_{\rm int}$. For example, for the $V_{\rm I}$ system, there are even greater variations between $E_{\rm ad}$ and $E_{\rm int}$, highlighting a wider range of adsorption possibilities depending on the sites. In general, $E_{\rm int}$ consistently displays lower values compared to $E_{\rm ad}$ for all types of vacancies. Thus, the most stable adsorption sites vary depending on the system and the metal species. For example, the $V_{\rm Pb}$ model shows Ag favoring b', Au at b, Cu at h, and Ni at b. These site preferences highlight the role of the type of vacancy in the tuning of the adsorption landscape for TM, with Ni consistently exhibiting strong site-specific interactions.

Among TMs, Ni emerges as the most favorable for film adsorption, exhibiting stronger adsorption and interactions, suggesting a higher affinity for the surface. Except for the $V_{\rm I}$ models, a general trend of energetic stability is observed: Ni > Cu > Au > Ag. In the case of the $V_{\rm I}$ models, the trend shifts to Ni > Au > Cu > Ag, with Au and Cu showing intermediate interactions, while Ag shows the greatest instability. Thin films MAI exhibit the highest $E_{\rm ad}$ and $E_{\rm int}$ values, highlighting the pivotal role of TM surface adsorption in improving energy stability. In particular, surface relaxation exerts the strongest influence on metals such as Ag and Au, while its effect on Ni and Cu is comparatively less pronounced.

3.1.3. Stability of Subsurface TM Incorporation. In the context of subsurface substitution on the $V_{\rm MA}$ and $V_{\rm Pb}$ models, Ni emerges as the most stabilizing dopant, particularly when replacing Pb in the surface-near layer $(TM_{\rm s}^{\rm 1L})$. This configuration yields the most negative values among all cases examined, indicating robust incorporation and strong coupling with the perovskite lattice. The enhanced stabilization likely arises from the favorable electronic compatibility between Ni and the lead-halide environment, allowing effective orbital hybridization and minimal charge imbalance. This pronounced interaction contrasts with the more modest effects observed at the MA and I sites, underscoring the critical role of the inorganic framework in accommodating TM.

In addition to Ni, the incorporation of Cu provides the highest energetic stabilization, followed by Au and Ag. The latter two show smaller differences between $E_{\rm ad}$ and $E_{\rm int}$ for

both subsurface substitution and adsorption cases. Interestingly, both adsorption and substitution in the $V_{\rm I}$ models with Au result in enhanced energetic stability compared to the other TM. This suggests that Au forms stronger interactions with such models, likely due to its distinctive electronic configuration and relativistic effects, which promote orbital contraction and improved overlap. In TMs2L, constraints imposed on the bottom surface atoms affect the behavior of subsurface substitution, resulting in a lower energetic stability relative to TM in TM_s^{1L}. In addition, substitution at the MA site becomes energetically unfavorable, as evidenced by the increase in both $E_{\rm ad}$ and $E_{\rm int}$ compared to passivated models. This reduced stability is driven by a change in the local chemical environment; specifically, the displacement of the TM dopant toward the halide sites disrupts the neighboring PbI₆-octahedra, thus compromising the overall structural integrity of the film.

3.2. Energetic Stability via Formation Energies. To facilitate a direct comparison of the energy stability between the structures of each model, the formation energy $(E_{\rm F})$ is determined using the following equation

$$E_{\rm F} = E_{\rm tot}^{\rm TM/slab} - E_{\rm p} - \sum_{i} \mu_{i} n_{i} \tag{3}$$

where $E_{\mathrm{tot}}^{\mathrm{TM/slab}}$ represents the total energy of TM adsorption (Ni, Cu, Ag, and Au) on MAI, V_{MA} , V_{Pb} , and V_{I} perovskite thin films, and E_{p} denotes the total energy of the MAI system without TM adsorption. Each species is indexed by $i=\mathrm{Ag}$, Au, Cu, Ni, Pb, I and the molecule MA, with n_i representing the number of atoms or molecules inserted $(n_i>0)$ or removed $(n_i<0)$. The chemical potential μ_i corresponds to the total energy per atom of the pure bulk system of species i. For the case of MA, the chemical potential was calculated using the total energy of its precursor, methylammonium iodide (MAI). Figure 3 presents the values of E_{F} . For the adsorption

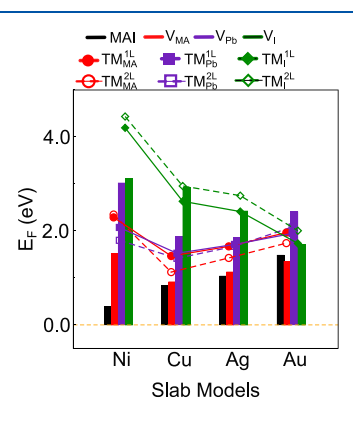


Figure 3. Formation energy $(E_{\rm F})$ for the most stable configuration of single-transition-metal adsorption (Ni, Cu, Ag, and Au) on MAI, $V_{\rm MA}$, $V_{\rm Pb}$, and $V_{\rm I}$ surface models, as well as for surface adsorption at MA, Pb, and I sites in the first $({\rm TM_s^{1L}})$ and second $({\rm TM_s^{2L}})$ layers of perovskite thin films.

scenarios, only the lowest energy site of $E_{\rm ad}$ and $E_{\rm int}$ are considered for each TM, while additional details are provided in the SI file.

For all models, positive values of $E_{\rm F}$ indicate that the incorporation of a TM, either by surface adsorption or by subsurface substitution at MA-Pb-I sites, requires external energy input, as the interaction between the TM and the surface MAPbI $_3$ is not inherently favorable. In particular, the

lower $E_{\rm F}$ values observed for the adsorption models suggest that these processes induce less structural perturbation than substitution, thus preserving the integrity of the lattice and making adsorption energetically more feasible. Across all TM, $E_{\rm F}$, increases in the presence of vacancies compared to the MAI surface. This indicates that vacancies generally destabilize TM adsorption, likely due to the disruption of the perovskite lattice and the loss of stabilizing interactions (e.g., bonding with Pb or I). The magnitude of this destabilization varies significantly depending on the type of vacancy and the TM, suggesting that the defect-TM interactions are highly specific.

The moderate increase in E_F for Ag, Au, and Cu within the $V_{
m MA}$ models indicates a localized destabilization, likely a consequence of the loss of hydrogen bonds or electrostatic interactions between MA and TM. In contrast, Ni shows a pronounced increase in E_F, underscoring its increased sensitivity to the absence of MA. This phenomenon can be attributed to the reduced ionic radius of Ni along with a higher charge density, which makes it more dependent on MA for stabilization. Similarly, $V_{\rm Pb}$ results in a notable destabilization across all TM, with Ni demonstrating the highest $E_{\rm F}$. Furthermore, $V_{\rm I}$ also contributes to substantial increases in $E_{\rm F}$, especially for Cu and Ni. This observation suggests that halide bonding is crucial in maintaining the stability of TM adsorption, and the removal of iodine considerably decreases the interaction strength between the TM and the perovskite surface.

3.3. Adsorption Site TM Preference. Furthermore, the negative values observed in $E_{\rm ad}$ and $E_{\rm int}$ indicate a stabilization of the system following TM adsorption or subsurface substitution, accompanied by energy release. It underscores the intricate nature of metal-surface interactions, where the initial formation stage is unfavorable as noted in $E_{\rm F}>0$, however, upon adsorption of the metal, the system is characterized by stronger interactions, leading to a more stable configuration. This highlights the necessity of considering both formation and adsorption energies to achieve a comprehensive understanding of these processes.

Therefore, assuming that adsorption begins from a free, isolated TM single atom, the negative adsorption energies indicate thermodynamically favorable processes. In contrast, the $E_{\rm F}$ reveal that adsorption starting from the bulk TM phase is energetically costly. Based on the analysis of energetic stability, we focused on the physicochemical characterization of the structures with the lowest $E_{\rm F}$, which are the most likely to occur. These include the adsorption cases of the MAI surface and the $V_{\rm MA}$, $V_{\rm Pb}$ and $V_{\rm I}$ defect models, as shown in Figure 4. In subsequent discussions, only the most stable adsorption site was considered.

3.4. Analysis of the TM–I Bonding. The surface adsorption of TM on perovskite thin films disrupts the local structural symmetry by drawing the metals closer to the terminal iodine atoms on the film surface. In most cases, a chemical bond is formed between the TM and the halides, with minimum bond distances $(d_{\min}^{\text{TM-I}})$ comparable to those observed in bulk transition metal halide salts, such as AgI, AuI, CuI, and NiI₂. The results $d_{\min}^{\text{TM-I}}$ are shown in Figure 5, we observed the smallest deviations in systems containing V_{MA} for all TM when comparing $d_{\min}^{\text{TM-I}}$ with their bulk counterparts. Among these, Au exhibited the smallest deviation, with a value of only 0.03 Å relative to the bulk AuI. Conversely, in the MAI, V_{Pb} , and V_{I} systems, Au demonstrated significantly larger deviations, with respective values of 0.31 Å, 0.20 Å, and 0.27 Å.

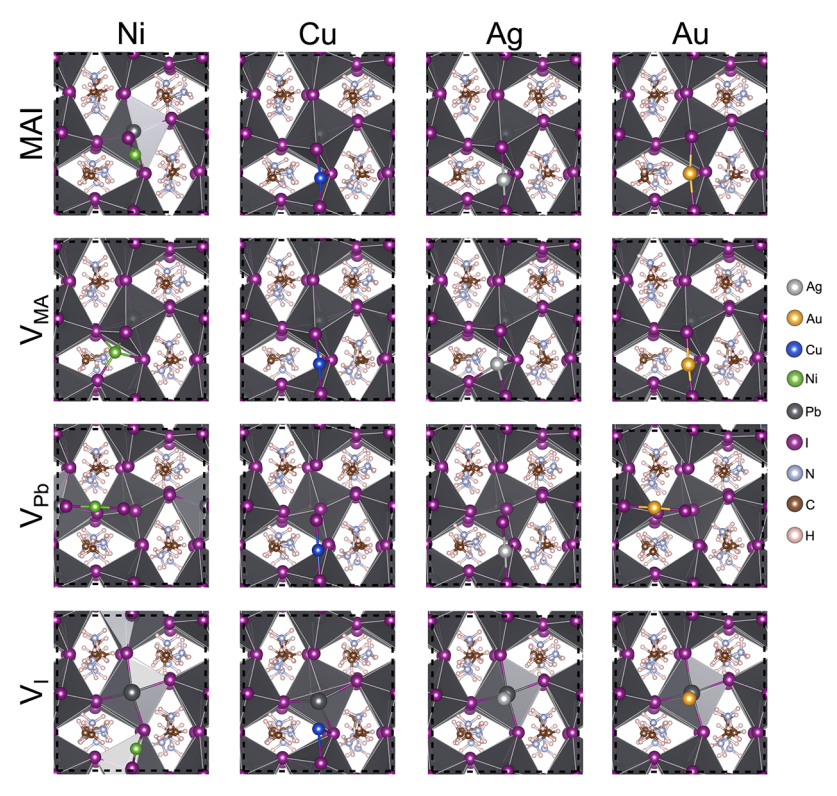


Figure 4. Top view of lowest energy configurations for single-transition metal adsorption (Ni, Cu, Ag, and Au) in MAI, $V_{\rm MA}$, $V_{\rm Pb}$ and $V_{\rm I}$ perovskite surfaces.

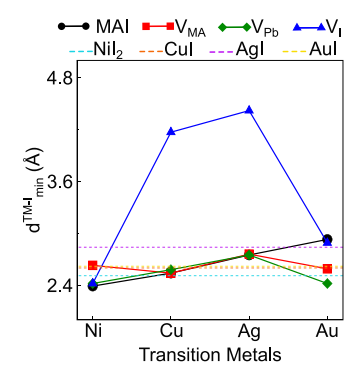


Figure 5. Minimum atomic distances between TM and iodides $(d_{\min}^{\mathrm{TM-I}})$ in MAI, V_{MA} , V_{Pb} and V_{I} perovskite surfaces. The dashed lines indicates the $d_{\min}^{\mathrm{TM-I}}$ values in the bulk phases of NiI₂, CuI, AgI, and AuI salts.

It should be noted that although the adsorption of Au on MAI and $V_{\rm MA}$ surfaces, considering the lowest energy configurations, occurs at similar adsorption sites, there is a significant difference in the $d_{\rm min}^{\rm TM-1}$ deviations relative to the bulk. Specifically, the deviations are 0.31 Å and 0.03 Å, respectively. This indicates a stronger interaction and closer proximity of the transition metal to the slab when surface vacancies are present. For example, in the $V_{\rm Pb}$ system, Au displays the shortest distance, indicating a favorable interaction. However, in the MAI system, Au exhibits one of the largest $d_{\rm min}^{\rm TM-I}$. This adaptability may be due to the electronic configuration of Au and its tendency to form more complex chemical interactions with the local environment.

Nickel consistently exhibits the shortest $d_{\min}^{\text{TM-I}}$ bond in all systems, indicating a significantly stronger interaction with iodine. This affinity can be attributed to the smaller atomic

radius of Ni and its electronic configuration, which favors a higher electron density at the interface, leading to stronger interactions. Moreover, both Ag and Cu are more sensitive to iodine vacancies, as evidenced by the largest increases in $d_{\min}^{\text{TM}-\text{I}}$ observed in the system with V_{I} . The absence of iodine atoms, which plays a crucial role in stabilizing TM–I interactions, appears to significantly hinder the adsorption of these metals. This can be explained by the more dispersive nature of the interactions Ag and Cu, which rely heavily on a complete chemical environment to achieve strong bonding.

We observed the formation of multiple chemical bonds between adsorbed TM and iodine atoms on MAPbI $_3$ surfaces containing $V_{\rm MA}$ vacancies, demonstrating a pronounced metal—iodine coordination capability. This multibonding behavior arises from the undercoordinated iodine atoms exposed by $V_{\rm MA}$ vacancies, which create accessible sites for metals to interact with several iodine neighbors simultaneously. The ability of such networks to form bonding networks underscores the high reactivity and strong binding affinity of these metals toward iodine in vacancy-rich environments, driven by the favorable orbital overlap between the metal states and the lone pairs of iodine.

3.5. Impact of Transition Metal Adsorption and Vacancies on Perovskite Charge Distribution. To enhance our atomistic understanding of the mechanism of interaction of TM with the slab models indicated by MAI, $V_{\rm MA}$, $V_{\rm Pb}$ and $V_{\rm I}$, we calculated the effective charges on each chemical species. For that, we used the electrostatic and chemical method derived from the density (DDEC)^{42,43} and the results are shown in Figure 6. As expected, the effective charges calculated by the DDEC framework consistently show that Pb retains a positive charge and I a negative charge for all TM/slab models. Although quantitative variations are

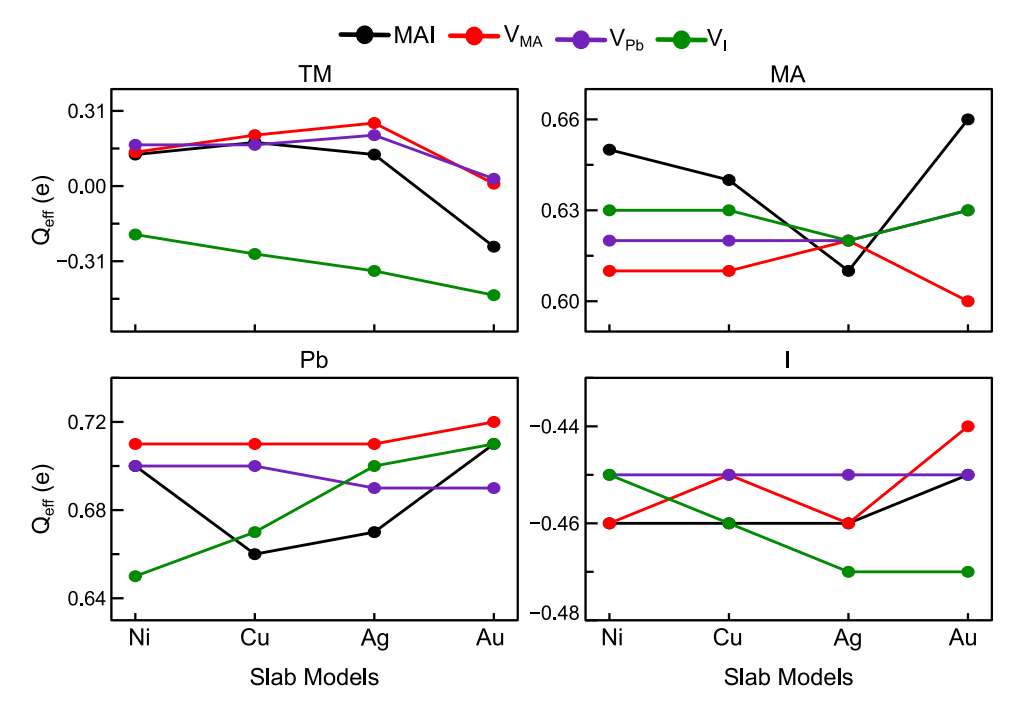


Figure 6. Effective DDEC charges (Q_{eff}) for TM (Ni, Cu, Ag, and Au), MA, Pb and I in MAI, V_{MA} , V_{Pb} and V_{I} perovskite surface models.

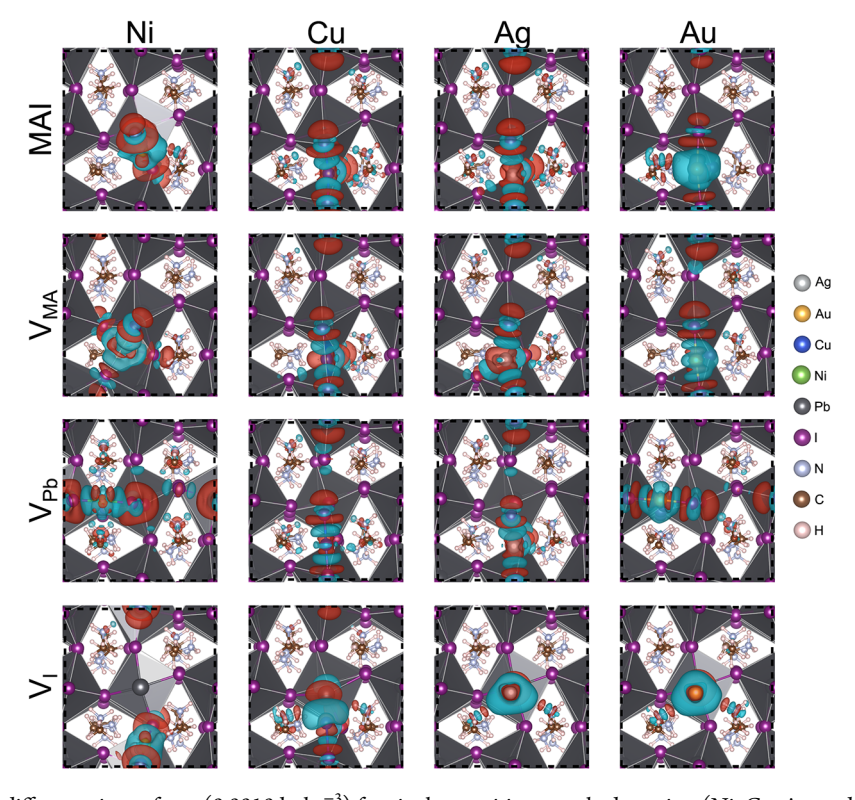


Figure 7. Electron density difference isosurfaces (0.0010 bohr⁻³) for single-transition metal adsorption (Ni, Cu, Ag, and Au) in MAI, $V_{\rm MA}$, $V_{\rm Pb}$, and $V_{\rm I}$ perovskite surfaces. The cyan and red regions indicate the accumulation and depletion of charge, respectively.

observed, reflecting local perturbations induced by the adsorbed TM, the large charge separation ($Q_{\rm eff}^{\rm Pb}-Q_{\rm eff}^{\rm I}$) indicates that the dominant ionic character of the PbI₆-octahedra framework is preserved.

For the MAI slab model (black lines in Figure 6), TM exhibits distinct charge states. As observed, Ag, Cu, and Ni generally show positive $Q_{\rm eff}$ values, indicating that they act as electron donors to the perovskite lattice. Specifically, Ni and

Cu maintain $Q_{\rm eff}$ around 0.15e and 0.2e, while Ag shows a slight increase peaking around 0.25e. In contrast, Au behaves as an electron acceptor, with $Q_{\rm eff}$ dropping significantly to approximately -0.2e indicating unique electronic interactions between this metal species and the perovskite framework.

In the presence of the $V_{\rm MA}$ slab model (red lines in Figure 6), the TM exhibits an increased positive charge compared with the MAI slab model, however, Au transitions to a nearly

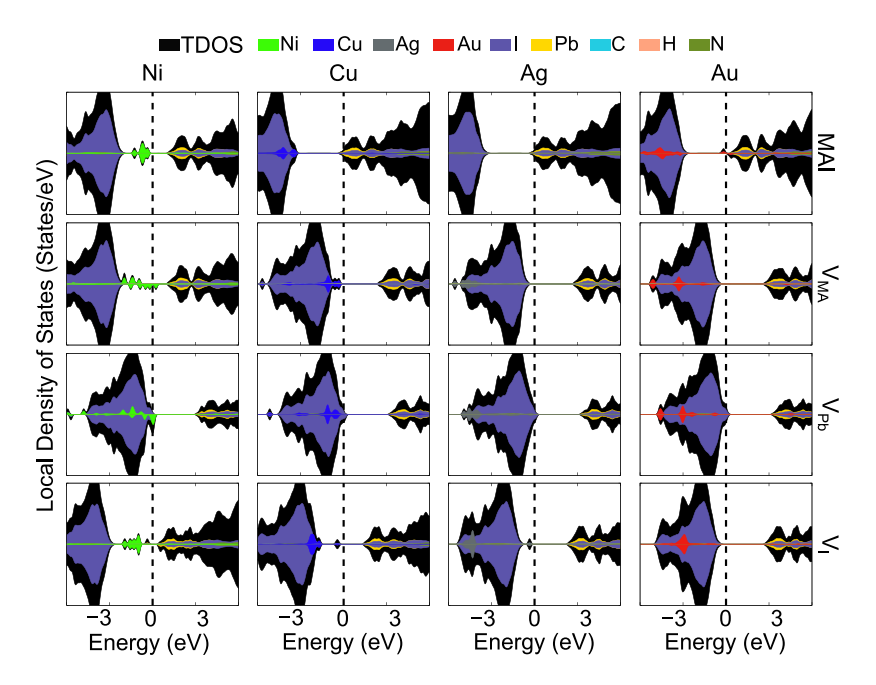


Figure 8. Local density of states for single-transition metal adsorption (Ni, Cu, Ag, and Au) in MAI, $V_{\rm MA}$, $V_{\rm Pb}$ and $V_{\rm I}$ perovskite surfaces, the valence band maximum (VBM) was set at 0 eV (vertical dashed line) and energy range considered spans from -70 to 70 eV for all plots.

neutral state (around 0.05e), it effectively loses its electronaccepting behavior. This suggests that the removal of MA strengthens the electron-donating tendencies of Ag, Cu, and Ni while decreasing the distinct role of Au. For $V_{\rm Pb}$ (purple lines in Figure 6), TM exhibit minimal variations in charge distribution. This indicates that Pb vacancies have a negligible impact on charge transfer dynamics concerning the TM, largely preserving the overall electronic environment of the MAI system.

In contrast, for TM adsorption in the $V_{\rm I}$ slab models (green lines in Figure 6), we observe a significant change in TM charges. All metals (particularly Ni, Cu, Ag, and Au) acquire a net negative charge, with $Q_{\rm eff}$ consistently dropping from approximately -0.15e for Ni to about -0.3e for Au. This transition suggests that $V_{\rm I}$ induces a charge transfer reversal, causing Ni, Cu, Ag, and Au to function as electron acceptors rather than donors.

3.6. Electron Density Redistribution via Electron Density Difference. To elucidate the binding mechanism of TM adsorption on perovskite thin-film surfaces, we analyzed the electron density difference using the following equation

$$\Delta \rho = \rho^{\text{TM+slab}} - \rho^{\text{TM}} - \rho^{\text{slab}} \tag{4}$$

where $\rho^{\rm TM+slab}$ is the total electron density of the TM adsorption on the MAI, $V_{\rm MA}$, $V_{\rm Pb}$ and $V_{\rm I}$ models, ρ is the electron density of the isolated TM and $\rho^{\rm slab}$ is the electron density of each frozen model, that is, both are fragments obtained from the TM+slab models in their optimized geometric positions. The results are shown in Figure 7.

The results reveal charge accumulation and depletion along the TM-I bonds, indicating significant charge redistribution upon adsorption. This behavior suggests a modulation of the electronic structure driven by metal-surface interactions, where charge transfer enhances bond polarization and influences the local chemical environment. The accumulation of charges around Au confirms its role as a charge acceptor in all the investigated models. In particular, such accumulation in

Au, considering the $V_{\rm Pb}$ and $V_{\rm MA}$ models, exhibits a reduced isosurface, indicating a lower redistribution of charges. As expected, charge accumulations are also observed around the halides (I⁻) near the TM, influenced by $d_{\rm min}^{\rm TM-I}$. Additionally, in the $V_{\rm I}$ model, charge accumulation is evident near all TM.

In contrast, we find decreases of charge around the Ag, Cu, and Ni in the MAI, $V_{\rm MA}$ and $V_{\rm Pb}$ models. This indicates a stronger Lewis acid character compared to the $V_{\rm I}$ case, corresponding to a charge transfer from the TM to the halides. All observations in Figure 7 are consistent with an effective charge analysis using DDEC. In addition, charge accumulation and depletion occur in MA molecules near TM–I interactions, revealing charge transfer dynamics from MA to halides through the NH $_{\rm 3}$ group, as observed in various MAPbI $_{\rm 3}$ -based perovskite thin films. The Specifically, we observed charge depletion near one of the H atoms in the NH $_{\rm 3}$ group, identifying it as the most acidic hydrogen and a potential charge transfer center.

3.7. Characterization of the Electronic States via the Local Density of States. The binding mechanism revealed that TM adsorption in MAPbI₃ thin films modulates the electronic properties. To elucidate these effects, we examined the local density of states (LDOS), as shown in Figure 8. In MAI, Ag and Cu a pronounced shift of the Fermi level ($E_{\rm Fermi}$) into the conduction band minimum (CBM), indicating a n-type character that improves electron density is observed. Au, in contrast, positions $E_{\rm Fermi}$ near the CBM while introducing localized Au-derived states close to this region, suggesting a partial hybridization with the conduction band. Moreover, Ni exhibits a distinctly different behavior, with $E_{\rm Fermi}$ aligning closer to the valence band maximum (VBM) and Ni derived states contributing prominently near this region, indicating a potential p-type character upon incorporation of Ni.

The introduction of $V_{\rm MA}$ further modifies these trends, particularly for Ni, where spin-down states emerge within the bandgap, with $E_{\rm Fermi}$ positioned at their center. This behavior suggests the formation of midgap trap states, which could act

as charge recombination centers, potentially affecting the optoelectronic properties. For Ag, Au, and Cu we found a shift of $E_{\rm Fermi}$ toward the VBM, indicating an enhanced hole concentration. However, Cu uniquely introduces Cu-derived states near the VBM, potentially modifying charge-transport mechanisms.

In the case of $V_{\rm Pb}$, Ag, Au, and Cu stabilize the electronic structure by placing $E_{\rm Fermi}$ within the VBM, suggesting minimal perturbation of the band gap. Ni follows a similar trend but contributes Ni-related states within the VBM, which may influence charge carrier mobility and recombination dynamics. In contrast, the presence of $V_{\rm I}$ induces deeper perturbations, with Ag and Cu introducing states within the bandgap, the former closer to the VBM. Au, while shifting $E_{\rm Fermi}$ toward the VBM, avoids the formation of midgap states, indicating a relatively benign electronic interaction. However, for Ni, it demonstrates a unique response, with midgap states appearing and $E_{\rm Fermi}$ aligning near the CBM, further underscoring its distinct electronic behavior among the metals studied.

Furthermore, it is important to note that while the PBE functional is generally effective for describing trends in the electronic properties of these materials, it is also well-established that it systematically underestimates absolute band gap values. Accordingly, our reported gaps should be considered a reliable qualitative guide rather than a precise quantitative measure.

3.8. Work Function Characterization. Modulation of the work function (Φ) induced by TM adsorption on MAPbI₃(100) surfaces is a crucial factor in optimizing the electronic properties of perovskite-based optoelectronic devices. Consequently, the induced change in the work function $(\Delta\Phi)$ is defined as the differential value between $\Phi^{\text{TM+slab}}$ and Φ^{slab} . The findings of $\Phi^{\text{TM+slab}}$ and $\Delta\Phi$ are depicted in Figure 9. The calculated values $\Delta\Phi$ for the MAI surfaces demonstrate a significant reduction in TM adsorption,

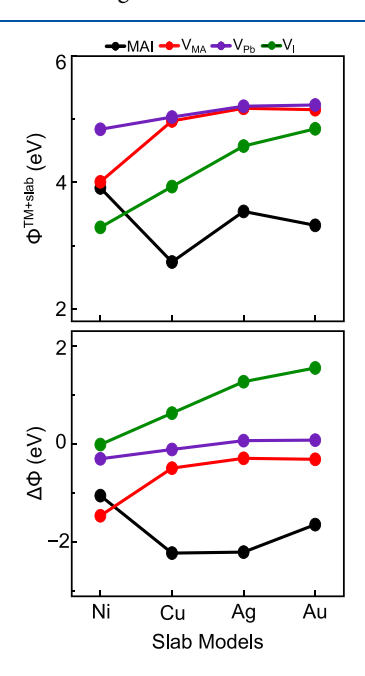


Figure 9. Top panel shows the work function $(\Phi^{\mathrm{TM+slab}})$, while the bottom panel displays the induced change in work function $(\Delta\Phi)$ for single-transition metal adsorption (Ni, Cu, Ag, and Au) in MAI, V_{MA} , V_{Pb} and V_{I} perovskite surfaces.

ı

with the most pronounced effect observed for Cu, followed sequentially by Ag and Au to a lesser degree.

In contrast, Ni shows the highest $\Phi^{\text{TM+slab}}$ among the metals under investigation, maintaining a value closer to MAI, with a standard deviation of approximately 0.52 between Φ^{slab} and Φ^{Ni} . This implies a comparatively moderate impact on the electronic structure compared to that of other metals. These trends are consistent with the LDOS analysis, where the location of E_{Fermi} within the CBM is associated with the significant reduction in $\Phi^{\text{TM+slab}}$ observed for the MAI system. This phenomenon suggests that the introduced metals primarily act as electron donors, thereby effectively reducing the surface electron extraction barrier.

For systems with vacancies, $\Delta\Phi$ exhibits a significant increase, suggesting stabilization of the surface and an elevated electron extraction barrier. In the presence of $V_{\rm MA}$ and $V_{\rm Pb}$, all the values of $\Phi^{\rm TM+slab}$ remain close to 5 eV, indicating that the removal of MA or Pb leads to a more electronically stable configuration. However, for $V_{\rm I}$, a higher value is observed in $\Delta\Phi$, with Cu and Ni showing the lowest values, which may stem from defect states that alter surface potential and effectively increase Φ . In contrast, Ag and Au exhibit higher $\Phi^{\rm TM+slab}$, suggesting that these metals can mitigate the electronic perturbations associated with iodine vacancies, potentially improving the properties of interfacial charge transport.

For the $V_{\rm MA}$, $V_{\rm Pb}$, and $V_{\rm I}$ models, we observe a monotonic increase in Φ with the increasing atomic number of adsorbed TM. Such effects can be attributed to interfacial charge redistribution and electrostatic interactions. Heavier metals, such as Au, tend to withdraw more electronic density from the perovskite surface or polarize it more strongly, thus raising the vacuum level and consequently Φ . This trend reflects the combined influence of metal electronegativity, d-orbital occupation, and the resulting dipole at the metal-perovskite surface interface.

4. CORRELATED INSIGHTS: THE INTERPLAY OF SURFACE MORPHOLOGY, WORK FUNCTION, AND CHARGE REDISTRIBUTION

Here, we initially present experimental data derived from field emission gun scanning electron microscopy (FEG-SEM) and energy-dispersive X-ray spectroscopy (EDS) analyses to evaluate the morphological and compositional characteristics of the perovskite films. Subsequently, we offer comprehensive theoretical insights on the influence of TM species on the determination of film morphology. Furthermore, we will also discuss the correlations between the effective atomic charges and Φ in the various scenarios investigated in this study.

4.1. Experimental Validation from FEG-SEM and EDS Analyses. To gain deeper insights into the nature of TM interactions on the surface of MAPbI₃, we complemented our DFT results with experimental characterization. Field-emission gun SEM and EDS were employed to analyze the surface morphology and elemental composition of the films. Details of the experimental methodology and additional analyzes are provided in the SI file. As shown in the SEM images and EDS maps of each TM (Figure 10), Ni exhibits a more uniform distribution across the perovskite film surface following the deposition of a 4 nm-thick TM layer, compared to the other transition metals. This shows a greater adsorption and interaction of this metal with the film surface. These experimental data support the theoretical findings of improved

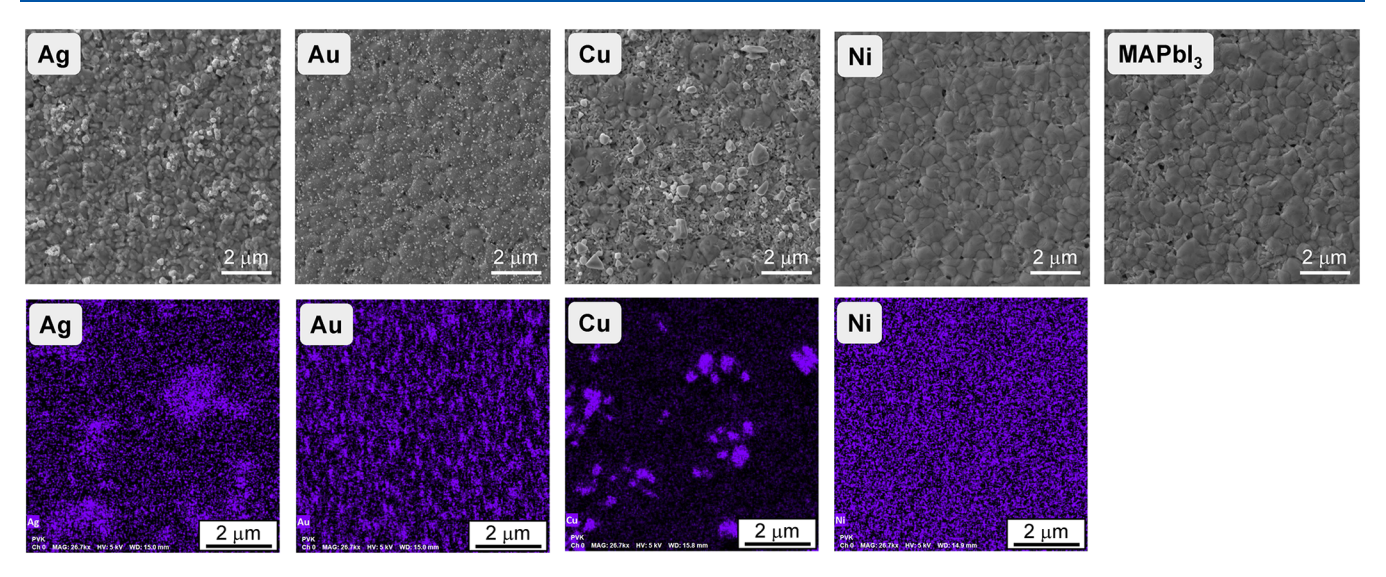


Figure 10. Scanning electron microscopy images (top panel) and energy dispersive spectroscopy analysis (bottom panel) of MAPbI₃ perovskite thin films, before and after deposition of a 4 nm thick layer of different metals: Ni, Cu, Ag, and Au.

energetic stability, where Ni was shown to exhibit lower $E_{\rm ad}$ and $E_{\rm int}$ values.

In contrast, both Cu and Ag show a pronounced tendency to coalesce into large metallic agglomerates that are unevenly distributed throughout the film surface, indicating a lower affinity for these metals for MAPbI₃. Interestingly, the experimentally observed homogeneity of the metal coverage follows the sequence Ni > Au > Cu > Ag, which mirrors the energetic stability trend predicted by our model $V_{\rm I}$ and suggests an iodine-deficient perovskite surface. A preliminary EDS analysis of the bare film yields a Pb/I ratio of 1.5:2.5, supporting this hypothesis (see experimental data in the SI file).

4.2. Work Function Modulation by Effective Charge.

To elucidate the primary factors that influence the modulation of the work function, we conducted an analysis of the correlations between Φ and the effective charges of adsorbed TM and the constituent ions of the perovskite (Pb, I, and MA). This correlative investigation encompassed our four different surface scenarios: MAI, $V_{\rm MA}$, $V_{\rm Pb}$, and $V_{\rm I}$, with the results presented in Figure 11.

Charge redistribution and Φ modulation upon TM adsorption are found to have a complex and multifactorial relationship for the MAI surface. The charge of the lead atoms shows the strongest, albeit still moderate, as demonstrated by

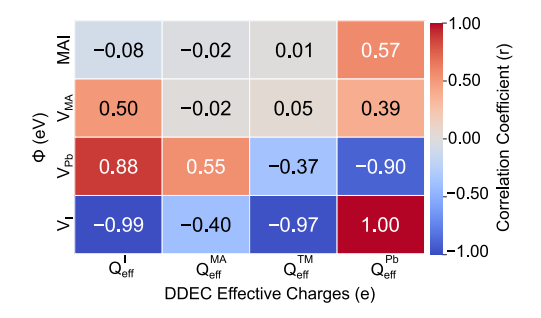


Figure 11. Correlation between the work function (Φ) and the effective DDEC charges from TM (Ni, Cu, Ag, and Au) and Pb, respectively $Q_{\rm eff}^{\rm TM}$ and $Q_{\rm eff}^{\rm Pb}$, considering the MAI, $V_{\rm MA}$, $V_{\rm Pb}$ and $V_{\rm I}$ perovskite surfaces models.

the Pearson correlation coefficients, which are generally weak. On an defect-free surface, no single atomic species acts as a straightforward and dominant predictor of Φ , as evidenced by nearly zero correlations with TM, iodide, and methylammonium charges. This implies that the electronic response to various adsorbates on an ideal lattice is a complex interaction between geometric relaxation, local bonding, and collective polarization effects that deviates from a straightforward linear trend.

However, the $V_{\rm I}$ model dramatically illustrates how the introduction of surface defects fundamentally transforms this complex electronic landscape into a highly predictable system. In this scenario, we found strong negative correlations between Φ and TM charges and iodine ions, indicating that as TM becomes more positive, greater charge transfer occurs from the TM to the surface, thus decreasing Φ . Furthermore, we found a nearly perfect positive correlation between effective charges Pb and Φ . This remarkable result suggests that $V_{\rm I}$ forms an extremely active electronic site, an undercoordinated Pb atom, which serves as the center of all charge transfer. The charges in Pb, I, and TM become tightly coupled variables in a coherent physical process, in which the charge state of the Pb atom emerges as a direct descriptor of the surface's work function.

An examination of cation vacancies further underscores the specificity of defect-mediated electronic modulation. In the $V_{\rm Pb}$ model, as the Pb charges on the surface become more positive, the values of Φ tend to increase because the more positive Pb nucleus attracts electrons from the surface; consequently, more energy is required to remove these electrons. In contrast, the $V_{\rm MA}$ model shows only weak to moderate correlations, similar to that of the clean surface. This indicates that, although the organic cation plays a minor role in the electronic structure, its absence does not create a predominant localized state that affects the TM adsorption in the same way as inorganic vacancies do. Therefore, surface vacancies actively control the response of the work function to adsorbates, with $V_{\rm I}$ acting as a strong linearizing agent for charge transfer effects.

In addition, while charge transfer is central to our analysis, the work function modulation is also influenced by structural perturbations, such as adsorbate-induced surface rumpling and local strain.⁴⁸ It is also important to note that our calculations

correspond to the low-coverage limit, i.e., single-atom approach; at higher coverages, adsorbate—adsorbate interactions are expected to significantly impact the reported trends. ^{23,30}

Overall, the experimental observations from SEM and EDS align closely with the theoretical insights gained from the work function—charge correlation analysis. In particular, the uniform Ni coverage observed experimentally is consistent with the prediction of the $V_{\rm I}$ model that under-coordinated Pb atoms act as strong electronic anchoring sites, promoting substantial charge transfer from the TM to the surface. This enhanced charge transfer reduces the work function and increases interfacial stability, as reflected by lower values of $E_{\rm ad}$ and $E_{\rm int}$ considering Ni. In contrast, the tendency of Cu and Ag to form large agglomerates experimentally matches their weaker correlations in the $V_{\rm I}$ scenario and their reduced electronic coupling with the defective surface. The general trend of experimental coverage (Ni > Au > Cu > Ag) mirrors the theoretical stability sequence predicted for surfaces deficient in iodine, strengthening the role of the $V_{\rm I}$ sites as dominant mediators of both the morphological and electronic response of the perovskite to TM deposition.

5. CONCLUSIONS

We performed density functional theory calculations, along with experimental characterizations using scanning electron microscopy and energy-dispersive X-ray spectroscopy techniques, to characterize the effects of surface adsorption and subsurface substitution of transition metals such as Ni, Cu, Ag, and Au on the pristine and defected MAPbI₃(100) surfaces.

Our results demonstrate that the adsorption and interaction energies of TM are highly dependent on both the metal species and the specific adsorption or subsurface substitution site. Among the elements studied, Ni consistently exhibits the strongest interactions across all systems, which we attribute to its smaller ionic radius and higher charge density, promoting stronger bonding with the perovskite surface. Vacancies play a crucial role in modulating the adsorption landscape, with V_{MA} and $V_{\rm I}$ vacancies inducing the most significant changes in both adsorption stability and electronic structure. This behavior is corroborated by experimental data, where the Ni layer deposited on top of a perovskite film is more evenly distributed across the surface compared to the other TM. Importantly, the $E_{\rm F}$ analysis reveals that subsurface substitution in the TM_s^{1L} and TM_s^{2L} layers is thermodynamically less favorable than surface adsorption. However, the observed stabilization through strong TM-surface interactions highlights the need to consider both formation and adsorption energies when evaluating subsurface substitution mechanisms in perovskite materials.

The structural analysis highlights the formation of TM–I bonds, with bond distances comparable to those of TM bulk halide salts. The Ni, in particular, exhibits the shortest $d_{\min}^{\text{TM}-1}$, indicative of its strong affinity for iodine. This is further corroborated by the electron density difference and effective charge analyses, which reveal significant charge redistribution and electron transfer between the TM and the perovskite surface. LDOS and Φ calculations provide additional insight into the electronic modifications induced by TM adsorption. While Ag, Au, and Cu tend to shift E_{Fermi} toward the conduction band, indicating donor-like behavior, Ni introduces midgap states that could influence charge recombination dynamics. Φ further demonstrates that TM adsorption generally reduces the electron extraction barrier, with Cu

showing the most substantial effect in MAI systems. However, the presence of vacancies, particularly $V_{\rm I}$, increases Φ , suggesting stabilization of the electronic surface environment.

Experimental characterization using FEG-SEM and EDS shows that the Ni atoms exhibit the most homogeneous distribution on the MAPbI $_3$ film surface, in contrast to the pronounced clustering observed for Cu and Ag. This uniform coverage strongly correlates with our first-principles predictions, which identified Ni as the specie with the highest surface interaction strength among the investigated transition metals. The observed sequence of metal dispersion (Ni > Au > Cu > Ag) also agrees with the trend of simulated energetic stability, particularly under conditions deficient in iodine modeled by the surface $V_{\rm L}$ further strengthening the consistency between theory and experiment.

In the context of solar energy harvesting, perovskite-based devices are composed of multiple functional layers, making the migration of metal species from contact layers across interfaces unavoidable. Such migration can potentially trigger degradation mechanisms. This work elucidates the interaction of transition metals with perovskite surfaces under low-concentration conditions, enabling the assessment of the impact of metal incorporation into perovskite regions and revealing the contrasting behaviors of different metals. These insights inform future device design, either by guiding the selection of metal species used in adjacent layers or by identifying electronic property signatures associated with metal incorporation into the perovskite phase, which represents an advance in this field.

ASSOCIATED CONTENT

Data Availability Statement

The data used for the figures, as well as additional analyzes, experimental data and technical details, are reported in the Supporting Information File.

Supporting Information

The Supporting Information is available free of charge at https://pubs.acs.org/doi/10.1021/acs.jpcc.5c04429.

Technical details of the selected PAW projectors; parameters for calculating adsorption energy ($E_{\rm ad}$) and interaction energy ($E_{\rm int}$) for the V_{MA} model; the electronic band structure of quasi-2D, and top view of single-transition metal adsorption (Ni,Cu, Ag, and Au) in MAI perovskite surfaces (PDF)

AUTHOR INFORMATION

Corresponding Author

Juarez L. F. Da Silva — São Carlos Institute of Chemistry, University of São Paulo, São Carlos, SP 13560-970, Brazil; orcid.org/0000-0003-0645-8760; Email: juarez dasilva@iqsc.usp.br

Authors

Israel C. Ribeiro – São Carlos Institute of Chemistry, University of São Paulo, São Carlos, SP 13560-970, Brazil; o orcid.org/0000-0002-5272-8752

Andreia de Morais — Center for Information Technology Renato Archer—CTI, Campinas, SP 13069-901, Brazil Lucas G. Chagas — Department of Physics, Federal University of São Carlos, São Carlos, SP 13565-905, Brazil; orcid.org/0000-0002-9653-6648 Jilian N. de Freitas — Center for Information Technology Renato Archer—CTI, Campinas, SP 13069-901, Brazil; o orcid.org/0000-0002-6446-1127

Ramiro M. dos Santos — São Carlos Institute of Chemistry, University of São Paulo, São Carlos, SP 13560-970, Brazil; orcid.org/0000-0002-4387-1223

Matheus P. Lima — Department of Physics, Federal University of São Carlos, São Carlos, SP 13565-905, Brazil; orcid.org/0000-0001-5389-7649

Complete contact information is available at: https://pubs.acs.org/10.1021/acs.jpcc.5c04429

Funding

The Article Processing Charge for the publication of this research was funded by the Coordenacao de Aperfeicoamento de Pessoal de Nivel Superior (CAPES), Brazil (ROR identifier: 00x0ma614).

Notes

The authors declare no competing financial interest.

ACKNOWLEDGMENTS

The authors appreciate the support from FAPESP (São Paulo Research Foundation, Brazil, Grant Numbers 2017/11631-2, 2018/21401-7, 2022/09312-4, 2017/11986-5, 2023/10395-4, and 2024/08610-7), Shell and the strategic importance of the support provided by ANP (Brazil's National Oil, Natural Gas and Biofuels Agency) through the R&D levy regulation. I.C.R. thanks the National Council for Scientific and Technological Development (CNPq) for the Ph.D. fellowship, grant number 140015/2021-3. M.P.L. gratefully acknowledges financial support from the CNPq (Brazilian National Council for Scientific and Technological Development) Grand Number 314169/2023-7. The authors are also grateful for the infrastructure provided to our computer cluster by the Department of Information Technology—Campus São Carlos.

ABBREVIATIONS

DFT density functional theory VASP Vienna Ab Initio Simulation Package PBE Perdew—Burke—Ernzerhof

REFERENCES

- (1) Kojima, A.; Teshima, K.; Shirai, Y.; Miyasaka, T. Organometal Halide Perovskites as Visible-Light Sensitizers for Photovoltaic Cells. *J. Am. Chem. Soc.* **2009**, *131*, 6050–6051.
- (2) Zheng, Y.; Li, Y.; Zhuang, R.; Wu, X.; Tian, C.; Sun, A.; Chen, C.; Guo, Y.; Hua, Y.; Meng, K.; Wu, K.; Chen, C.-C. Towards 26% Efficiency in Inverted Perovskite Solar Cells via Interfacial Flipped Band Bending and Suppressed Deep-level Traps. *Energy Environ. Sci.* 2024, 17, 1153–1162.
- (3) Ye, J.; Mondal, N.; Carwithen, B. P.; Zhang, Y.; Dai, L.; Fan, X.-B.; Mao, J.; Cui, Z.; Ghosh, P.; Otero-Martínez, C.; van Turnhout, L.; Huang, Y.-T.; Yu, Z.; Chen, Z.; Greenham, N. C.; Stranks, S. D.; Polavarapu, L.; Bakulin, A.; Rao, A.; Hoye, R. L. Z. Extending the Defect Tolerance of Halide Perovskite Nanocrystals to Hot Carrier Cooling Dynamics. *Nat. Commun.* **2024**, *15*, No. 8120.
- (4) De Wolf, S.; Holovsky, J.; Moon, S.-J.; Löper, P.; Niesen, B.; Ledinsky, M.; Haug, F.-J.; Yum, J.-H.; Ballif, C. Organometallic Halide Perovskites: Sharp Optical Absorption Edge and Its Relation to Photovoltaic Performance. *J. Phys. Chem. Lett.* **2014**, *5*, 1035–1039.
- (5) Scalon, L.; Szostak, R.; Araujo, F. L.; Adriani, K. F.; Silveira, J. F. R. V.; Oliveira, W. X. C.; Da Silva, J. L. F.; Oliveira, C. C.; Nogueira, A. F. Improving the Stability and Efficiency of Perovskite Solar Cells by a Bidentate Anilinium Salt. *JACS Au* **2022**, *2*, 1306–1312.

- (6) Leng, K.; Abdelwahab, I.; Verzhbitskiy, I.; Telychko, M.; Chu, L.; Fu, W.; Chi, X.; Guo, N.; Chen, Z.; Chen, Z.; Zhang, C.; Xu, Q.-H.; Lu, J.; Chhowalla, M.; Eda, G.; Loh, K. P. Molecularly Thin Two-dimensional Hybrid Perovskites with Tunable Optoelectronic Properties Due to Reversible Surface Relaxation. *Nat. Mater.* **2018**, *17*, 908–914.
- (7) Ghosh, S.; Mukhopadhyay, S.; Paul, S.; Pradhan, B.; De, S. K. Control Synthesis and Alloying of Ambient Stable Pb-Free $Cs_3Bi_2Br_9(1-x)I_9x$ (0 $\leq x \leq 1$) Perovskite Nanocrystals for Photodetector Application. *ACS Appl. Nano Mater.* **2020**, 3, 11107–11117.
- (8) Filip, M. R.; Eperon, G. E.; Snaith, H. J.; Giustino, F. Steric Engineering of Metal-Halide Perovskites with Tunable Optical Band Gaps. *Nat. Commun.* **2014**, *5*, No. 5757.
- (9) Paritmongkol, W.; Dahod, N. S.; Stollmann, A.; Mao, N.; Settens, C.; Zheng, S.-L.; Tisdale, W. A. Synthetic Variation and Structural Trends in Layered Two-dimensional Alkylammonium Lead Halide Perovskites. *Chem. Mater.* **2019**, *31*, 5592–5607.
- (10) Li, Z.; Yang, M.; Park, J.-S.; Wei, S.-H.; Berry, J. J.; Zhu, K. Stabilizing Perovskite Structures by Tuning Tolerance Factor: Formation of Formamidinium and Cesium Lead Iodide Solid-State Alloys. *Chem. Mater.* **2016**, 28, 284–292.
- (11) Srikanth, M.; Ozório, M. S.; Da Silva, J. L. F. Optical and dielectric properties of lead perovskite and iodoplumbate complexes: an ab initio study. *Phys. Chem. Chem. Phys.* **2020**, *22*, 18423–18434.
- (12) Ozório, M. S.; Srikanth, M.; Besse, R.; Da Silva, J. L. F. The Role of the A-cations in the Polymorphic Stability and Optoelectronic Properties of Lead-Free ASnI₃ Perovskites. *Phys. Chem. Chem. Phys.* **2021**, 23, 2286–2297.
- (13) da Silva Filho, J. M. C.; de Morais, A.; Cesar, R. R.; Joanni, E.; Teixeira, R. C.; Marques, F. C.; de Freitas, J. N. Investigation of the Stability of Metallic grids for Large-Area Perovskite Solar Cells. *Sol. Energy Mater. Sol. Cells* **2024**, 276, No. 113043.
- (14) Rani, M.; Khan, M. M.; Numan, A.; Khalid, M.; Abbas, S. M.; Iqbal, M.; Mansoor, M. A. Breaking Barriers: Addressing Challenges in Perovskite Solar Cell Development. *J. Alloys Compd.* **2025**, *1010*, No. 177648.
- (15) Li, Z.; Klein, T. R.; Kim, D. H.; Yang, M.; Berry, J. J.; van Hest, M. F. A. M.; Zhu, K. Scalable Fabrication of Perovskite Solar Cells. *Nat. Rev. Mater.* **2018**, *3*, No. 18017.
- (16) Qiu, L.; He, S.; Ono, L. K.; Liu, S.; Qi, Y. Scalable Fabrication of Metal Halide Perovskite Solar Cells and Modules. *ACS Energy Lett.* **2019**, *4*, 2147–2167.
- (17) Swartwout, R.; Hoerantner, M. T.; Bulović, V. Scalable Deposition Methods for Large-area Production of Perovskite Thin Films. *Energy Environ. Mater.* **2019**, *2*, 119–145.
- (18) da Silva Filho, J. M. C.; Gonçalves, A. D.; Marques, F. C.; de Freitas, J. N. A Review on the Development of Metal Grids for the Upscaling of Perovskite Solar Cells and Modules. *Sol. RRL* **2022**, *6*, No. 2100865.
- (19) Zhang, W.; Xiong, J.; Wang, S.; Liu, W.-e.; Li, J.; Wang, D.; Gu, H.; Wang, X.; Li, J. Highly Conductive and Transparent Silver Grid/Metal Oxide Hybrid Electrodes for Low-Temperature Planar Perovskite Solar Cells. *J. Power Sources* **2017**, 337, 118–124.
- (20) Wang, J.; Chen, X.; Jiang, F.; Luo, Q.; Zhang, L.; Tan, M.; Xie, M.; Li, Y.-Q.; Zhou, Y.; Su, W.; Li, Y.; Ma, C.-Q. Electrochemical Corrosion of Ag Electrode in the Silver Grid Electrode-Based Flexible Perovskite Solar Cells and the Suppression Method. *Sol. RRL* **2018**, *2*, No. 1800118
- (21) Duarte, V. C. M.; Ivanou, D.; Bernardo, G.; Andrade, L.; Mendes, A. Embedded Current Collectors for Efficient Large Area Perovskite Solar Cells. *Int. J. Energy Res.* **2022**, *46*, 5288–5295.
- (22) Yang, Y.; Min, F.; Qiao, Y.; Li, Z.; Vogelbacher, F.; Liu, Z.; Lv, W.; Wang, Y.; Song, Y. Embossed Transparent Electrodes Assembled by Bubble Templates for Efficient Flexible Perovskite Solar Cells. *Nano Energy* **2021**, *89*, No. 106384.
- (23) Lin, Y.; Shao, Y.; Dai, J.; Li, T.; Liu, Y.; Dai, X.; Xiao, X.; Deng, Y.; Gruverman, A.; Zeng, X. C.; Huang, J. Metallic Surface Doping of Metal Halide Perovskites. *Nat. Commun.* **2021**, *12*, No. 7.

- (24) Hohenberg, P.; Kohn, W. Inhomogeneous Electron Gas. *Phys. Rev.* 1964, 136, No. B864.
- (25) Kohn, W.; Sham, L. J. Self-consistent Equations Including Exchange and Correlation Effects. *Phys. Rev.* **1965**, *140*, No. A1133.
- (26) Perdew, J. P.; Burke, K.; Ernzerhof, M. Generalized Gradient Approximation Made Simple. *Phys. Rev. Lett.* **1996**, 77, No. 3865.
- (27) Song, R.; Zhao, R. Density Functional Theory Study of Two-Dimensional Hybrid Organic-Inorganic Perovskites: Frontier Level Alignment and Chirality-Induced Spin Splitting. *AAPPS Bull.* **2024**, 34, No. 20.
- (28) dos Santos, R. M.; Ornelas-Cruz, I.; Dias, A. C.; Lima, M. P.; Da Silva, J. L. F. Theoretical Investigation of the Role of Mixed A⁺ Cations in the Structure, Stability, and Electronic Properties of Perovskite Alloys. *ACS Appl. Energy Mater.* **2023**, *6*, 5259–5273.
- (29) Ribeiro, I. C.; Moraes, P. I. R.; Bittencourt, A. F. B.; Da Silva, J. L. F. Unveiling the Impact of Organic Cation Passivation on Structural and Optoelectronic Properties of Two-Dimensional Perovskites Thin Films. *Appl. Surf. Sci.* **2024**, *678*, No. 161098.
- (30) Lima, M. P.; Caturello, N. A. M. S.; Da Silva, J. L. F. Ab initio Investigation of the Interface Between $Mo_{10}S_{24}$ Nanoflakes and the Au(111) Surface: Interplay Between Interaction Energy and Morphology. *Appl. Surf. Sci.* **2022**, *604*, No. 154413.
- (31) González, J. E.; Besse, R.; Lima, M. P.; Da Silva, J. L. F. Decoding Van der Waals Impact on Chirality Transfer in Perovskite Structures: Density Functional Theory Insights. *J. Chem. Inf. Model.* **2024**, *64*, 1306–1318.
- (32) Qin, Y.; Zhong, H.; Intemann, J. J.; Leng, S.; Cui, M.; Qin, C.; Xiong, M.; Liu, F.; Jen, A. K.-Y.; Yao, K. Coordination Engineering of Single-Crystal Precursor for Phase Control in Ruddlesden—Popper Perovskite Solar Cells. *Adv. Energy Mater.* **2020**, *10*, No. 1904050.
- (33) Moraes, P. I. R.; Bittencourt, A. F. B.; Andriani, K. F.; Da Silva, J. L. F. Theoretical Insights into Methane Activation on Transition-Metal Single-Atom Catalysts Supported on the CeO₂(111) Surface. *J. Phys. Chem. C* **2023**, *127*, 16357–16366.
- (34) Li, P.; Yan, L.; Cao, Q.; Liang, C.; Zhu, H.; Peng, S.; Yang, Y.; Liang, Y.; Zhao, R.; Zang, S.; Zhang, Y.; Song, Y. Dredging the Charge-Carrier Transfer Pathway for Efficient Low-Dimensional Ruddlesden-Popper Perovskite Solar Cells. *Angew. Chem., Int. Ed.* **2023**, *62*, No. e202217910.
- (35) Ribeiro, I. C.; Picoli, F. D.; Moraes, P. I. R.; Fonseca, A. F. V.; Oliveira, L. N.; Nogueira, A. F.; Da Silva, J. L. F. Impact of Thin Film Thickness on the Structural, Energetic and Optoelectronic Properties of Two-Dimensional $\text{FPEA}_2(\text{MA}_{n-1})\text{Pb}_n\text{I}_{3n+1}$ Perovskites. *ACS Appl. Energy Mater.* **2025**, *8*, 3346–3359.
- (36) Grimme, S.; Antony, J.; Ehrlich, S.; Krieg, H. A Consistent and Accurate Ab Initio Parametrization of Density Functional Dispersion Correction (dft-d) for the 94 Elements H-pu. *J. Chem. Phys.* **2010**, 132, No. 154104.
- (37) Blöchl, P. E. Projector Augmented-wave Method. Phys. Rev. B 1994, 50, No. 17953.
- (38) Kresse, G.; Joubert, D. From Ultrasoft Pseudopotentials to the Projector Augmented-wave Method. *Phys. Rev. B* **1999**, 59, No. 1758.
- (39) Kresse, G.; Hafner, J. Ab Initio Molecular Dynamics for Liquid Metals. *Phys. Rev. B* **1993**, *47*, No. 558.
- (40) Kresse, G.; Furthmüller, J. Efficient Iterative Schemes for Ab initio Total-energy Calculations Using a Plane-wave Basis set. *Phys. Rev. B* **1996**, *54*, No. 11169.
- (41) Francis, G. P.; Payne, M. C. Finite Basis Set Corrections to Total Energy Pseudopotential Calculations. *J. Phys.: Condens. Matter* **1990**, 2, 4395–4404.
- (42) Manz, T. A.; Limas, N. G. Introducing DDEC6 Atomic Population Analysis: Part 1. Charge Partitioning Theory and Methodology. *RSC Adv.* **2016**, *6*, 47771–47801.
- (43) Limas, N. G.; Manz, T. A. Introducing DDEC6 atomic Population Analysis: Part 2. Computed Results for a Wide Range of Periodic and Nonperiodic Materials. *RSC Adv.* **2016**, *6*, 45727–45747.
- (44) Wang, D.; Han, D.; Li, X.-B.; Xie, S.-Y.; Chen, N.-K.; Tian, W. Q.; West, D.; Sun, H.-B.; Zhang, S. B. Determination of Formation

- and Ionization Energies of Charged Defects in Two-Dimensional Materials. *Phys. Rev. Lett.* **2015**, *114*, No. 196801.
- (45) Zhang, C.; Yan, L.; Qiu, C.; Zhang, C.-X.; Shen, T.; Wei, S.-H.; Deng, H.-X. Correcting charged supercell defect calculations in low-dimensional semiconductors. *Phys. Rev. B* **2023**, *108*, No. 245305.
- (46) Kröger, F. A.; Nachtrieb, N. H. The Chemistry of Imperfect Crystals. *Phys. Today* **1964**, *17*, 66–69.
- (47) Ribeiro, I. C.; Moraes, P. I. R.; Bittencourt, A. F. B.; Da Silva, J. L. F. Role of the Adsorption of Alkali Cations on Ultrathin n-Layers of Two-Dimensional Perovskites. *J. Phys. Chem. C* **2023**, 127, 13667—13677
- (48) Singh-Miller, N. E.; Marzari, N. Surface energies, work functions, and surface relaxations of low-index metallic surfaces from first principles. *Phys. Rev. B* **2009**, *80*, No. 235407.

